

Topological X -states in a quantum impurity model

Moallison F. Cavalcante,^{1,2,*} Marcus V. S. Bonança,² Eduardo Miranda,² and Sebastian Deffner^{1,3}

¹*Department of Physics, University of Maryland, Baltimore County, Baltimore, MD 21250, USA*

²*Gleb Wataghin Physics Institute, The University of Campinas, 13083-859, Campinas, São Paulo, Brazil*

³*National Quantum Laboratory, College Park, MD 20740, USA*

(Dated: January 30, 2025)

Topological qubits are inherently resistant to noise and errors. However, experimental demonstrations have been elusive as their realization and control is highly complex. In the present work, we demonstrate the emergence of topological X -states in the long-time response of a locally perturbed quantum impurity model. The emergence of the double-qubit state is heralded by the lack of decay of the response function as well as the out-of-time order correlator signifying the trapping of excitations, and hence information in local edge modes.

Introduction Recent years have seen the rapid development of more and more advanced quantum computing platforms. Leading technologies are based on a variety of physical platforms [1], such as ion traps [2], neutral atoms [3], entangled photons [4], or superconducting circuits [5]. A uniquely distinct approach is based on leveraging the topological properties of complex quantum many-body systems and the resulting anyonic statistics of the quasiparticle excitations [6].

In the present work, we demonstrate the emergence of a topological X -state in an impurity model. Notably, this *topological double-qubit* is realized in the stationary state of the local edge modes, and hence it is a consequence of the topology of the quantum many-body system. In contrast to more conventional topological qubits, however, our X -state is not characterized by anyonic statistics, but rather by the nonequilibrium response of the perturbed system.

Understanding the nonequilibrium dynamics of closed, one-dimensional quantum many-body systems is a challenging problem. Due to the inherent complexity that emerges from the interaction between the many degrees of freedom, general descriptions accounting for universal dynamical phenomena is a rather involved problem [7–9]. Therefore, it is paramount to investigate models that exhibit analytical, or partially analytical, solutions, where more controllable and in-depth studies can be developed. In this direction, quantum impurity models have attracted significant attention in the literature [10–19].

Here, we study the dynamical response of a quantum impurity model, namely, the transverse-field quantum Ising chain with an impurity at its edge [14]. Such an impurity gives rise to a rich phase diagram, where new boundary phases, with up to two localized edge states, emerge, see Fig. 1 below. We show that these edge modes can be accessed through the local control of the impurity and that they hinder the perfect spread of energy and information throughout the chain. In other words, for a suitable finite-time control protocol, excitations can be introduced in the chain through the impurity and a part of them gets trapped in the localized modes. After relaxation, the state describing the remaining excitations can take the form of

two entangled qubits, also known as an X -state [20]. This opens the possibility of using this setup for information-processing purposes.

Quantum impurity model We start by describing the system. We consider an interacting quantum system, namely, a spin-1/2 chain with open boundary conditions described by the following Hamiltonian,

$$H_0 = -J \sum_{j=1}^{N-1} \sigma_j^x \sigma_{j+1}^x - Jh \sum_{j=2}^N \sigma_j^z - Jh\mu \sigma_1^z, \quad (1)$$

where $\sigma_j^{a=x,y,z}$ are the Pauli matrices (two times the spin-1/2 operators) at the site j , $J \equiv 1$ is the exchange coupling, $h > 0$ is the external field magnitude and $\mu \neq 1$ plays the role of an impurity at the edge. Typically, we will assume that $N \rightarrow \infty$.

This model was introduced and analytically solved in Ref. [14]. In Suppl. Mat. [21], we provide the main details of this solution. The authors of Ref. [14] have shown that the presence of the edge impurity, $\mu \neq 1$, produces a new localized mode at the edge $j = 1$, beyond the well-studied Majorana zero mode (MZM) found by Kitaev in the impurity-free case, $\mu = 1$ [22]. Although slightly different from the transverse field quantum Ising chain, the model in Eq. (1) still undergoes a quantum phase transition, when (for $J = 1$) h is changed and crosses the critical value $h_c \equiv 1$ [14]. For values $h < h_c$ and $h > h_c$, the system is found in the ferromagnetic and paramagnetic phases, respectively.

We highlight that, different from the delocalized (bulk) modes, the two localized edge modes, which hereafter we will denote by $\gamma_{1,2}$, *only* appear in specific regions of the (h, μ) -phase diagram. Along the line $\mu = 1$, we recover a physics reminiscent of the Kitaev chain [23]: for $h < 1$, the mode γ_1 exists (topological phase), while for $h > 1$ only the delocalized modes are present (trivial phase). For $\mu \neq 1$, the impurity effects appear. The mode γ_1 is still present for all μ in the whole ferromagnetic side. Concerning the mode γ_2 , it can appear in two different regions, depending on the values of (h, μ) . These two regions are: $h > 1$ and $|\mu| < \sqrt{1 - 1/h}$, and, $\forall h$ and $|\mu| > \sqrt{1 + 1/h}$.

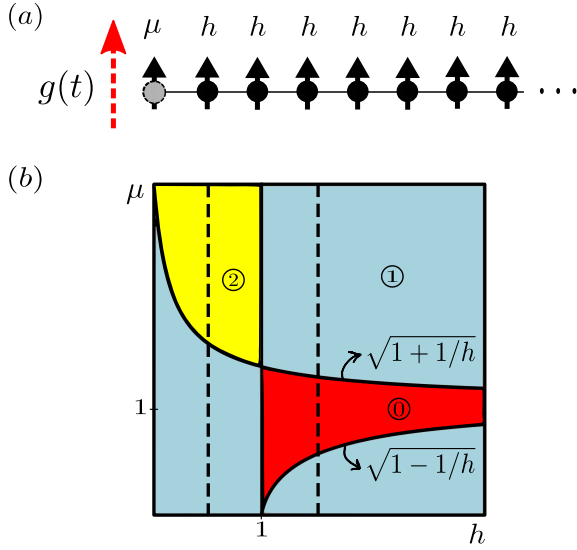


FIG. 1. (a) Sketch of the model in Eq. (1). The impurity (μ) is described by the gray ball. The large red arrow represents the finite-time control $g(t)$ acting at the impurity site. (b) (h, μ) -phase diagram [14]. The different colored regions highlight the number of localized modes close to the edge $j = 1$: zero in the red region, one in the light blue region, and two in the yellow region. The two dashed black lines indicate two values of the control parameter h , namely, $h = 1/2$ and $3/2$, which we will use later on in order to cover all the boundary phases.

Figure 1 summarizes this information as follows: in the light blue regions, we only have one localized mode, either γ_1 or γ_2 , while in the yellow region we have both localized modes. Finally, in the red region, only the delocalized modes are present. Furthermore, it is important to stress that the $\gamma_{1,2}$ modes have very different physical origins. While the γ_2 mode appears as a direct consequence of an inhomogeneity in real space, the γ_1 mode has a topological origin, and thus is topologically protected [23–25]. The real-time dynamics of such localized edge states has been experimentally investigated in [26].

In its diagonal form, the Hamiltonian in Eq. (1) reads,

$$H_0 = \sum_{\kappa} \Gamma_{\kappa} \gamma_{\kappa}^{\dagger} \gamma_{\kappa}. \quad (2)$$

In the latter equation, summation over κ includes both localized, $\gamma_{1,2}$, and delocalized, γ_k , fermionic modes. The ground state $|\mathbf{0}\rangle$ of the Hamiltonian (1) is the fermionic vacuum of γ_{κ} , thus $\gamma_{\kappa}|\mathbf{0}\rangle = 0$ for all κ . In the Suppl. Mat. [21], we provide explicit expressions for the dispersions Γ_{κ} .

Local control and response function We now turn to the response of the system to finite-time control localized at $j = 1$. Assuming that the chain is initialized in the ground state $|\mathbf{0}\rangle$ (which is a zero-temperature equilibrium state) for arbitrary values of (h, μ) , we apply an impulse $g(t) = -g_0 \delta(t) \sigma_1^z$ at the impurity (where $\delta(\cdot)$ denotes the Dirac delta function).

This perturbation drives the system out of equilibrium and injects energy. An experimentally accessible quantity [27] is the response function,

$$\Phi(t, \mu) = \frac{i}{2^3} \langle [\sigma_1^z(t), \sigma_1^z(0)] \rangle_0, \quad (3)$$

where $\sigma_1^z(t) = e^{iH_0 t} \sigma_1^z e^{-iH_0 t}$ is the operator σ_1^z in the Heisenberg representation [28] and $\langle \cdots \rangle_0 \equiv \langle \mathbf{0} | \cdots | \mathbf{0} \rangle$. For a sufficiently small value of g_0 , the impulse is weak and the response function (3) describes how $\langle \sigma_1^z(t) \rangle$ evolves [29]. In the following, we will show that the local monitoring of the system at the impurity provides important information about the nonequilibrium dynamics of the considered model in its different boundary phases.

Firstly, we consider the short-time behavior of $\Phi(t, \mu)$. For very short times $t \ll J^{-1}$, we expand the operator $\sigma_1^z(t)$ in powers of Jt to obtain $\Phi(t \ll J^{-1}, \mu) \propto t$, regardless of the point in the (h, μ) -phase diagram. In other words, the short-time behavior of the response function does not distinguish the different boundary phases.

To obtain intermediate and long-time behaviors of $\Phi(t, \mu)$, we use the diagonal form (2) of the Hamiltonian H_0 . This allows us to perform the calculation of the expectation value in Eq. (3), yielding

$$\Phi(t, \mu) = \sum_{\kappa, \kappa'} f_{\kappa \kappa'} \sin[(\Gamma_{\kappa} + \Gamma_{\kappa'})t]. \quad (4)$$

The amplitude $f_{\kappa \kappa'}$ is the probability of finding the system in the two-particle state $|\kappa \kappa'\rangle = \gamma_{\kappa}^{\dagger} \gamma_{\kappa'}^{\dagger} |\mathbf{0}\rangle$ after the previously described perturbation. It reads, $f_{\kappa \kappa'} = v_{\kappa} u_{\kappa'} (v_{\kappa} u_{\kappa'} - v_{\kappa'} u_{\kappa})$, with $u_{\kappa} = u_k$ and $v_{\kappa} = v_k$ for the delocalized modes and $u_{\kappa} = u^{(\ell)}$ and $v_{\kappa} = v^{(\ell)}$ for $\gamma_{\ell=1,2}$. These are wave functions at the edge, $j = 1$, for the different modes, see Suppl. Mat. [21] to find explicit expressions.

The colored curves in Fig. 2 show Eq. (4) for different values of μ and for the values of h corresponding to the dashed black lines in Fig. 1. Figures 2(a, b) depict the results for the paramagnetic phase, $h > 1$. After an initially linear growth, around $t \approx J^{-1}$, the response function starts to decrease as an oscillatory function with a power-law envelope. In the regions with only one localized mode (the γ_2 mode), a slower relaxation is observed for $\Phi(t, \mu)$, that is, it tends to zero according to $t^{-3/2}$. Figures 2(a, b) also show a faster decay of $\Phi(t, \mu)$ along the boundaries $\mu = \sqrt{1 \pm 1/h}$, $\Phi(t, \mu) \sim t^{-2}$, even though the γ_2 mode is absent. Deep inside the red region of Fig. 1, we have a t^{-3} scaling for $\Phi(t, \mu)$.

Figure 2(c) shows the results for the ferromagnetic phase, $h < 1$. In the region where only the mode γ_1 is present, the scaling behavior $t^{-3/2}$ is exactly the same as that observed in the paramagnetic region (when γ_2 exists). This tells us that the long-time decay of the response function is not affected by the physical origin of the localized mode. Similarly to the paramagnetic side, the power-law decay changes at the boundary between two different

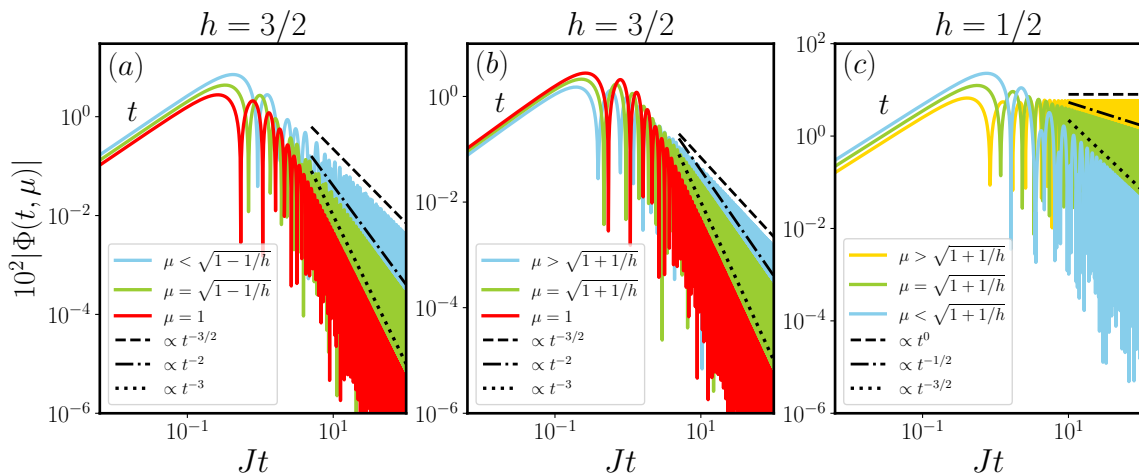


FIG. 2. Response function (4) for different μ and for two values of h . For very short times $t \ll J^{-1}$, we can see the general t growth. In (a), (b) and (c), we go through the different boundary phases: (a) and (b) correspond to the paramagnetic side while (c) to the ferromagnetic one (see Fig. 1). The dashed, dashed-dotted and dotted black lines represent the power-law decays obtained from stationary phase approximation (see Suppl. Mat. [21] for details).

phases. Along $\mu = \sqrt{1+1/h}$, a much slower decay can be observed, that is, $\Phi(t \gg J^{-1}, \mu) \sim t^{-1/2}$. Again, the impurity effects can be detected by the response function even when the mode γ_2 (which is a direct consequence of it) is absent.

Deep inside the yellow region of Fig. 1, both modes $\gamma_{1,2}$ contribute to the response function. In Fig. 2(c), we notice their drastic effect on $\Phi(t \gg J^{-1}, \mu)$: it no longer decays to zero but instead oscillates indefinitely. In fact, we obtain

$$\Phi(t \gg J^{-1}, \mu) \propto \sin \Gamma^{(2)}t + \mathcal{O}(t^{-3/2}), \quad (5)$$

where $\Gamma^{(2)}$ is the energy of the mode γ_2 (since the mode γ_1 has zero energy, $\Gamma^{(1)} = 0$). This coherent oscillation in the long-time limit appears after the delocalized modes undergo relaxation, and so the dynamics is effectively governed only by the two edge modes. In summary, the response function (3) already shows that local monitoring of the system response detects the partial trapping of excitations injected by the local control.

The previously discussed power-law behaviors can be obtained analytically considering the stationary phase approximation (SPA) [30]. Suppl. Mat. [21] summarizes our results.

In Ref. [18], the authors have obtained similar results, but for a different quantum impurity model. This suggests that only the number of localized edge modes, and no other microscopic details, dominates the long-time behavior of the two-time autocorrelation function (3).

Measuring the spread of correlations We continue the analysis with a commonly used quantifier of information scrambling [31, 32]. The so-called out-of-time order correlation (OTOC) function is given by

$$\mathcal{C}(t, \mu) = \frac{1}{2} \langle |[\sigma_1^z(t), \sigma_1^z(0)]|^2 \rangle_0. \quad (6)$$

Note that the OTOC (6) depends on the choice of operators [33, 34]. Here, we have chosen a local one to emphasize once again that the local monitoring of the system can give relevant information about the nonequilibrium dynamics. Although similar to the response function (3), it has been shown that the OTOC carries much more information about the spread of quantum correlations, even in non-chaotic systems [16, 35–41].

It is easy to see that $\mathcal{C}(t, \mu) = 1 - \text{Re}\{F(t, \mu)\}$, with

$$F(t, \mu) = \langle \sigma_1^z(t) \sigma_1^z(0) \sigma_1^z(t) \sigma_1^z(0) \rangle_0, \quad (7)$$

where the out-of-time order structure becomes evident (and $\text{Re}\{\cdot\}$ denotes the real part). In complete analogy to the response function, the short-time behavior of the OTOC is independent of the region in the (h, μ) -diagram. In fact, one can show that for short times $t \ll J^{-1}$, the OTOC (6) grows according to, $\mathcal{C}(t \ll J^{-1}, \mu) \propto t^2$, independent of μ and h . This behavior clearly emphasizes the slow, nonexponential spread of information. The impurity model (1) does not support quantum chaos.

To obtain intermediate and long-time behaviors, the calculation of the expectation value in Eq. (6) is more conveniently performed introducing the Majorana representation, a_j, b_j , such that the spin operator at the impurity site can be rewritten as $\sigma_1^z = ia_1 b_1$, and so $F(t, \mu) = \langle a_1(t) b_1(t) a_1(t) b_1(t) a_1(t) b_1(t) a_1(t) b_1(t) \rangle_0$. As shown in Ref. [36], we can cast the above expectation value in the form of the Pfaffian of a matrix whose elements are defined by the two-point correlation functions of the Majorana fermions a_1, b_1 : $G_{rr'}(t) = \langle r(t) r'(0) \rangle_0$, $r, r' = a_1, b_1$. All the details about the calculations are relegated to the Suppl. Mat. [21].

Figure 3 depicts the results for $\mathcal{C}(t, \mu)$. Regardless of the region in the (h, μ) -diagram, $\mathcal{C}(t, \mu)$ reaches a maximum value around $t \approx J^{-1}$, and for $t \gtrsim J^{-1}$ it transits

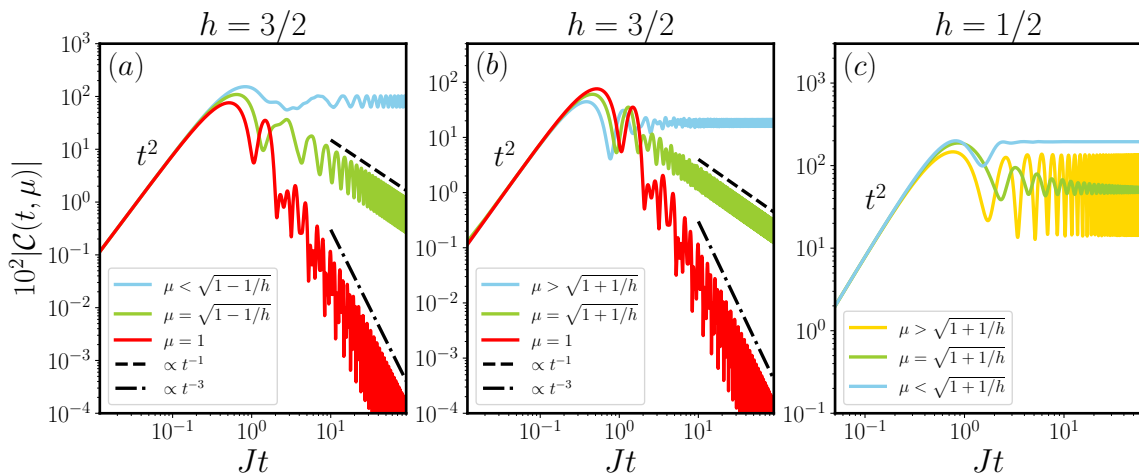


FIG. 3. OTOC in Eq. (6) for different values of μ and for two values of h . The general short-time growth t^2 for $t \ll J^{-1}$ is observed. Once again, in (a), (b) and (c) we go through the different boundary phases shown in Fig. 1. In (a) and (b), we show results on the paramagnetic side, while in (c) the ferromagnetic behaviors are shown. The dashed and dashed-dotted black lines in (a) and (b) represent two power-law decays (see Suppl. Mat. [21] for details).

to another behavior. When $t \gg J^{-1}$, we can see how the presence of the impurity modifies the behavior of the OTOC (6). In the paramagnetic phase, Figs. 3(a, b) show three distinct behaviors. First, without localized modes, $\mathcal{C}(t \gg J^{-1}, \mu)$ decays to zero according to t^{-3} , like the response function, cf. Figs. 2(a, b), showing a complete spread of the information as $Jt \rightarrow \infty$.

The effects of the edge mode γ_2 on the OTOC can already be seen along the boundaries $\mu = \sqrt{1 \mp 1/h}$ for $h > 1$. In Figs. 3(a, b), we observe that the information spreads more slowly, $\mathcal{C}(t \gg J^{-1}, \mu) \sim t^{-1}$, compared to the previous situation.

Inside the regions where only the mode γ_2 contributes, $h > 1$ and $\mu \leq \sqrt{1 \mp 1/h}$, the OTOC is given by the blue curves in Figs. 3(a, b). Interestingly, as time evolves, instead of a power-law decay, the OTOC remains *finite* for all times. In fact, for large t , we have

$$\mathcal{C}(t \gg J^{-1}, \mu) \propto 1 - (\text{const.}) \cos 2\Gamma^{(2)}t, \quad (8)$$

where const. is a (h, μ) -dependent constant. Hence, $\mathcal{C}(t \rightarrow \infty, \mu)$ is governed by γ_2 in the regions $h > 1$ and $\mu \leq \sqrt{1 \mp 1/h}$. This long-time nonzero value of the OTOC reflects how the localized character of the wave function of the mode γ_2 around the impurity prevents the perfect spread of the information (and energy) throughout the chain. Similar results have been obtained recently for other systems showing localized edge modes [16, 37, 38, 40] and for a system of interacting electrons in one-dimension [35].

Turning to the ferromagnetic side, $h < 1$, the results can be found in Fig. 3(c). Due to the presence of the mode γ_1 for all μ , we see that the OTOC remains finite throughout the ferromagnetic region. For $h < 1$ and $\mu \leq \sqrt{1 + 1/h}$, γ_1 is the only localized mode contributing to the OTOC. Since it has zero energy, $\mathcal{C}(t \gg J^{-1}, \mu)$

converges to a finite value, see Fig. 3(c). Finally, when $\mu > \sqrt{1 + 1/h}$ and $h < 1$, both modes $\gamma_{1,2}$ are present, and so the OTOC shows an oscillatory long-time behavior. The corresponding analytical result reads, $\mathcal{C}(t \gg J^{-1}, \mu) \propto 1 - (\text{const.}') \cos \Gamma^{(2)}t$, where const.' is another (h, μ) -dependent constant. The OTOC now oscillates with frequency $\Gamma^{(2)}$ (half of the frequency found in the paramagnetic phase with a single localized mode). This is essentially the only difference with respect to the case in which γ_2 was the only contribution.

Emergence of topological X-states The comparison between Figs. 2 and 3 clearly shows the complementary information provided by $\Phi(t, \mu)$ and $\mathcal{C}(t, \mu)$. The nonequilibrium steady state characterized by the response and OTOC functions unambiguously exhibits the trapping of excitations in the edge modes. The natural question arises whether the emerging state has useful and interesting properties.

The time evolution of the system, starting from the ground state $|\mathbf{0}\rangle$, after the perturbation $g(t) = -g_0\delta(t)\sigma_1^z$, is given by $\rho(t) = |\Psi(t)\rangle\langle\Psi(t)|$, where $|\Psi(t)\rangle = (\cos g_0\mathbf{1} + i \sin g_0 e^{-iH_0 t}\sigma_1^z)|\mathbf{0}\rangle$ (see Suppl. Mat. [21]). Motivated by the correspondence between the existence of the modes $\gamma_{1,2}$, the behavior of the response and OTOC functions, and the decay of coherences induced by the perturbation between states with different occupations of localized and delocalized modes (see Suppl. Mat. [21]), we trace out the delocalized modes to obtain the reduced density operator $\rho_{\text{loc}}(t) = \text{Tr}_{\text{del}} \rho(t)$, where Tr_{del} denotes the partial trace.

For the remainder of the analysis, we restrict ourselves to the yellow region of Fig. 1. As shown in the Suppl. Mat.

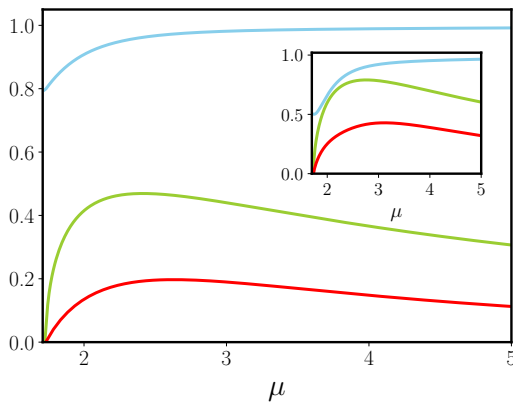


FIG. 4. Purity (blue), concurrence (green), and discord (red) for the X -state in Eq. (9). We used $h = 0.5$, so $\mu > 1.7321$ in order to remain in the yellow region of Fig. 1(b), and $g_0 = 0.5$. In the inset we show the same three quantities but for $g_0 = \pi/2$.

[21], $\rho_{\text{loc}}(t)$ then becomes

$$\rho_{\text{loc}}(t) = \begin{pmatrix} \rho_{11} & 0 & 0 & \rho_{14}(t) \\ 0 & \rho_{22} & \rho_{23}(t) & 0 \\ 0 & \rho_{23}^*(t) & \rho_{33} & 0 \\ \rho_{14}^*(t) & 0 & 0 & \rho_{44} \end{pmatrix}, \quad (9)$$

when written in the basis $\{|n_1, n_2\rangle = |0, 0\rangle, |1, 0\rangle, |0, 1\rangle, |1, 1\rangle\}$ (in this order), where $n_\ell = 0, 1$ is the number of excitations in the localized ℓ mode.

We see that $\rho_{\text{loc}}(t)$ is an X -state [20, 42–54]. This kind of double-qubit state describes a large and important class of entangled quantum states, ranging from pure Bell states to Werner mixed states [20]. In the present case, the qubits consist of combinations of states having zero, one or two fermionic excitations in the localized modes, namely, $|0, 0\rangle$ and $|1, 1\rangle$ for one qubit and $|1, 0\rangle$ and $|0, 1\rangle$ for another qubit.

For the quantum impurity model (1), the X -structure is a consequence of the fact that $\sigma_1^z|0\rangle$ yields states with two or zero excitation, but also couples the localized and delocalized modes. This allows for part of the excitations to relax and hence granting access to the 4-dimensional Hilbert space spanned by all possible occupations of the localized modes. Thus, this X -state form of $\rho_{\text{loc}}(t)$ cannot exist in the other regions of the (h, μ) -diagram.

In Fig. 4 we collect information theoretic characterizations [55], such as purity, concurrence, and discord, of $\rho_{\text{loc}}(t)$ (9) as a function of μ for fixed values of h and g_0 (see Suppl. Mat. [21] for other values). For $g_0 < 1$, the state is approximately pure and the quantum correlations quantified by the concurrence and discord have a non-monotonic behavior. Interestingly, both concurrence and discord reach a maximal value for small, but finite values of μ . In the non-perturbative regime, $g_0 > 1$, we see an enhancement of quantum correlations. For very large values of μ the quantum state becomes essentially classical.

Concluding remarks In the present analysis, we have shown the emergence of topological X -states in a quantum impurity model. This emergence is the consequence of the nonequilibrium response to a local perturbation, and it is heralded by the long-time behavior of the response function and OTOC. In two recent experimental works [56, 57], probing the nonequilibrium dynamics of Rydberg atomic chains, the authors were able to measure very similar OTOC as ours (6).

Finally, it is worth to highlight the similarity of our results and boundary time crystals (BTC) [58]. In our system, like in BTC, while the bulk undergoes relaxation, $\langle \sigma_{j \gg 1}^z(Jt \gg 1) \rangle = \sigma_{j \gg 1, \text{eq}}^z$, where $\sigma_{j \gg 1, \text{eq}}^z$ is the equilibrium bulk value before the perturbation, the boundary breaks time-translation symmetry, $\langle \sigma_{j \sim 1}^z(Jt \gg 1) \rangle = \varphi_j(t)$, where $\varphi_j(t)$ is a periodic function of time. A more detailed analysis of the potential emergence of BTC in impurity models is left for future work.

This work was supported by Conselho Nacional de Desenvolvimento Científico e Tecnológico (CNPq), Brazil, through grant No. 200267/2023-0. M.V.S.B. acknowledges the support of CNPq, under Grant No. 304120/2022-7. E.M. acknowledges the support of CNPq, under Grant No. 309584/2021-3. The work was also financed (M.V.S.B. and E.M.), in part, by the São Paulo Research Foundation (FAPESP), Brazil, Process Number 2022/15453-0. S.D. and M.F.C. acknowledge support from the John Templeton Foundation under Grant No. 62422.

* moallison@umbc.edu

- [1] B. C. Sanders, *How to Build a Quantum Computer*, 2399-2891 (IOP Publishing, 2017).
- [2] C. D. Bruzewicz, J. Chiaverini, R. McConnell, and J. M. Sage, Trapped-ion quantum computing: Progress and challenges, *Appl. Phys. Rev.* **6**, 021314 (2019).
- [3] K. Wintersperger, F. Dommert, T. Ehmer, A. Housanov, J. Klepsch, W. Maurer, G. Reuber, T. Strohm, M. Yin, and S. Luber, Neutral atom quantum computing hardware: performance and end-user perspective, *EPJ Quantum Technology* **10**, 32 (2023).
- [4] S. Slussarenko and G. J. Pryde, Photonic quantum information processing: A concise review, *Appl. Phys. Rev.* **6**, 041303 (2019).
- [5] O. Ezratty, Perspective on superconducting qubit quantum computing, *Eur. Phys. J. A* **59**, 94 (2023).
- [6] V. Lahtinen and J. K. Pachos, A Short Introduction to Topological Quantum Computation, *SciPost Phys.* **3**, 021 (2017).
- [7] B. Whaley and G. Milburn, Focus on coherent control of complex quantum systems, *New J. Phys.* **17**, 100202 (2015).
- [8] A. Soriani, E. Miranda, S. Deffner, and M. V. S. Bonança, Shortcuts to thermodynamic quasistaticity, *Phys. Rev. Lett.* **129**, 170602 (2022).
- [9] M. F. Cavalcante, M. V. S. Bonança, E. Miranda, and S. Deffner, Nanowelding of quantum spin- $\frac{1}{2}$ chains at minimal dissipation, *Phys. Rev. B* **110**, 064304 (2024).

- [10] R. Vasseur, K. Trinh, S. Haas, and H. Saleur, Crossover physics in the nonequilibrium dynamics of quenched quantum impurity systems, *Phys. Rev. Lett.* **110**, 240601 (2013).
- [11] D. M. Kennes, V. Meden, and R. Vasseur, Universal quench dynamics of interacting quantum impurity systems, *Phys. Rev. B* **90**, 115101 (2014).
- [12] R. Vasseur, J. P. Dahlhaus, and J. E. Moore, Universal nonequilibrium signatures of majorana zero modes in quench dynamics, *Phys. Rev. X* **4**, 041007 (2014).
- [13] M. Schiró and A. Mitra, Transport across an impurity in one-dimensional quantum liquids far from equilibrium, *Phys. Rev. B* **91**, 235126 (2015).
- [14] G. Francica, T. J. G. Apollaro, N. Lo Gullo, and F. Plastina, Local quench, majorana zero modes, and disturbance propagation in the ising chain, *Phys. Rev. B* **94**, 245103 (2016).
- [15] B. Bertini and M. Fagotti, Determination of the nonequilibrium steady state emerging from a defect, *Phys. Rev. Lett.* **117**, 130402 (2016).
- [16] B. Dóra, M. A. Werner, and C. P. Moca, Information scrambling at an impurity quantum critical point, *Phys. Rev. B* **96**, 155116 (2017).
- [17] H. Bragança, M. F. Cavalcante, R. G. Pereira, and M. C. O. Aguiar, Quench dynamics and relaxation of a spin coupled to interacting leads, *Phys. Rev. B* **103**, 125152 (2021).
- [18] U. Javed, J. Marino, V. Oganesyan, and M. Kolodrubetz, Counting edge modes via dynamics of boundary spin impurities, *Phys. Rev. B* **108**, L140301 (2023).
- [19] A. Larzul, A. M. Sengupta, A. Georges, and M. Schirò, Fast scrambling at the boundary, arXiv preprint, arXiv:2407.13617 (2024).
- [20] A. R. P. Rau, Algebraic characterization of x-states in quantum information, *Journal of Physics A: Mathematical and Theoretical* **42**, 412002 (2009).
- [21] Supplemental material.
- [22] Here we are using the fact that the one-dimensional transverse field quantum Ising chain, after the Jordan-Wigner transformation, can be mapped to a special case of the Kitaev chain [21, 59].
- [23] A. Y. Kitaev, Unpaired majorana fermions in quantum wires, *Physics-Uspekhi* **44**, 131 (2001).
- [24] J. Alicea, New directions in the pursuit of majorana fermions in solid state systems, *Reports on Progress in Physics* **75**, 076501 (2012).
- [25] W. DeGottardi, M. Thakurathi, S. Vishveshwara, and D. Sen, Majorana fermions in superconducting wires: Effects of long-range hopping, broken time-reversal symmetry, and potential landscapes, *Phys. Rev. B* **88**, 165111 (2013).
- [26] E. J. Meier, F. A. An, and B. Gadway, Observation of the topological soliton state in the su–schrieffer–heeger model, *Nature Communications* **7**, 13986 (2016).
- [27] M. Cheneau, P. Barmettler, D. Poletti, M. Endres, P. Schauß, T. Fukuhara, C. Gross, I. Bloch, C. Kollath, and S. Kuhr, Light-cone-like spreading of correlations in a quantum many-body system, *Nature* **481**, 484 (2012).
- [28] P. Coleman, *Introduction to Many-Body Physics* (Cambridge University Press, Cambridge, 2015).
- [29] R. Kubo, M. Toda, and N. Hashitsume, *Statistical Physics II: Nonequilibrium Statistical Mechanics*, Vol. 2 (Springer Berlin, Heidelberg, 1991).
- [30] Y.-H. Huang, Y.-T. Zou, and C. Ding, Dynamical relaxation of a long-range kitaev chain, *Phys. Rev. B* **109**, 094309 (2024).
- [31] D. A. Roberts and B. Swingle, Lieb-robinson bound and the butterfly effect in quantum field theories, *Phys. Rev. Lett.* **117**, 091602 (2016).
- [32] A. Touil and S. Deffner, Information scrambling – a quantum thermodynamic perspective, *EPL (Europhys. Lett.)* **146**, 48001 (2024).
- [33] A. Touil and S. Deffner, Quantum scrambling and the growth of mutual information, *Quantum Sci. Technol.* **5**, 035005 (2020).
- [34] D. Tripathy, A. Touil, B. Gardas, and S. Deffner, Quantum information scrambling in two-dimensional Bose-Hubbard lattices, *Chaos* **34**, 043121 (2024).
- [35] B. Dóra and R. Moessner, Out-of-time-ordered density correlators in luttinger liquids, *Phys. Rev. Lett.* **119**, 026802 (2017).
- [36] C.-J. Lin and O. I. Motrunich, Out-of-time-ordered correlators in a quantum ising chain, *Phys. Rev. B* **97**, 144304 (2018).
- [37] M. Sedlmayr, H. Cheraghi, and N. Sedlmayr, Information trapping by topologically protected edge states: Scrambling and the butterfly velocity, *Phys. Rev. B* **108**, 184303 (2023).
- [38] Q. Bin, L.-L. Wan, F. Nori, Y. Wu, and X.-Y. Lü, Out-of-time-order correlation as a witness for topological phase transitions, *Phys. Rev. B* **107**, L020202 (2023).
- [39] S. Kheiri, H. Cheraghi, S. Mahdavifar, and N. Sedlmayr, Information propagation in one-dimensional $xy-\Gamma$ chains, *Phys. Rev. B* **109**, 134303 (2024).
- [40] S. Sur and D. Sen, Effects of topological and non-topological edge states on information propagation and scrambling in a floquet spin chain, *Journal of Physics: Condensed Matter* **36**, 125402 (2023).
- [41] V. Muruganandam, M. Sajjan, and S. Kais, Defect-induced localization of information scrambling in 1d kitaev model, *Physica Scripta* **99**, 105123 (2024).
- [42] H. Ollivier and W. H. Zurek, Quantum discord: A measure of the quantumness of correlations, *Phys. Rev. Lett.* **88**, 017901 (2001).
- [43] T. Yu and J. H. Eberly, Finite-time disentanglement via spontaneous emission, *Phys. Rev. Lett.* **93**, 140404 (2004).
- [44] T. Yu and J. Eberly, Sudden death of entanglement: Classical noise effects, *Optics Communications* **264**, 393 (2006).
- [45] M. F. m. c. Santos, P. Milman, L. Davidovich, and N. Zagury, Direct measurement of finite-time disentanglement induced by a reservoir, *Phys. Rev. A* **73**, 040305 (2006).
- [46] A. Al-Qasimi and D. F. V. James, Sudden death of entanglement at finite temperature, *Phys. Rev. A* **77**, 012117 (2008).
- [47] M. S. Sarandy, Classical correlation and quantum discord in critical systems, *Phys. Rev. A* **80**, 022108 (2009).
- [48] M. Ali, A. R. P. Rau, and G. Alber, Quantum discord for two-qubit x states, *Phys. Rev. A* **81**, 042105 (2010).
- [49] F. Galve, G. L. Giorgi, and R. Zambrini, Maximally discordant mixed states of two qubits, *Phys. Rev. A* **83**, 012102 (2011).
- [50] Q. Chen, C. Zhang, S. Yu, X. X. Yi, and C. H. Oh, Quantum discord of two-qubit x states, *Phys. Rev. A* **84**, 042313 (2011).
- [51] X.-M. Lu, J. Ma, Z. Xi, and X. Wang, Optimal measurements to access classical correlations of two-qubit states, *Phys. Rev. A* **83**, 012327 (2011).

- [52] N. Quesada, A. Al-Qasimi, and D. F. James, Quantum properties and dynamics of x states, *Journal of Modern Optics* **59**, 1322 (2012).
- [53] Y. Huang, Quantum discord for two-qubit x states: Analytical formula with very small worst-case error, *Phys. Rev. A* **88**, 014302 (2013).
- [54] W. F. Balthazar, D. G. Braga, V. S. Lamego, M. H. M. Passos, and J. A. O. Huguenin, Spin-orbit x states, *Phys. Rev. A* **103**, 022411 (2021).
- [55] M. A. Nielsen and I. L. Chuang, *Quantum computation and quantum information* (Cambridge university press, 2010).
- [56] D.-S. Xiang, Y.-W. Zhang, H.-X. Liu, P. Zhou, D. Yuan, K. Zhang, S.-Y. Zhang, B. Xu, L. Liu, Y. Li, and L. Li, Observation of quantum information collapse-and-revival in a strongly-interacting rydberg atom array, arXiv:2410.15455 (2024).
- [57] X. Liang, Z. Yue, Y.-X. Chao, Z.-X. Hua, Y. Lin, M. K. Tey, and L. You, Observation of anomalous information scrambling in a rydberg atom array, arXiv:2410.16174 (2024).
- [58] F. Jemini, A. Russomanno, J. Keeling, M. Schirò, M. Dalmonte, and R. Fazio, Boundary time crystals, *Phys. Rev. Lett.* **121**, 035301 (2018).
- [59] S. Sachdev, *Quantum Phase Transitions* (Cambridge University Press, Cambridge, 1999).
- [60] E. Lieb, T. Schultz, and D. Mattis, Two soluble models of an antiferromagnetic chain, *Annals of Physics* **16**, 407 (1961).
- [61] W.-C. Yueh, Eigenvalues of several tridiagonal matrices, *Applied Mathematics E-Notes [electronic only]* **5**, 66 (2005).

SUPPLEMENTAL MATERIAL

In this Supplementary Material, we provide details on (i) the impurity model, (ii) the OTOC calculations, (iii) the long-time behaviors of the correlation functions, (iv) the reduced density state for the localized edge modes, and (v) the information characterization of our X -state.

MODEL

The open boundary condition spin-1/2 chain with an edge-impurity is described by the Hamiltonian [14]

$$H_0 = - \sum_{j=1}^{N-1} \sigma_j^x \sigma_{j+1}^x - h \sum_{j=2}^N \sigma_j^z - h\mu \sigma_1^z, \quad (10)$$

where $\sigma_j^{a=x,y,z}$ are the Pauli matrices at the site j and μ defines the impurity at the edge. After applying the Jordan-Wigner transformation [59, 60], $\sigma_j^+ = (\sigma_j^x + i\sigma_j^y)/2 = (-1)^j \exp\left(i\pi \sum_{i=1}^{j-1} c_i^\dagger c_i\right) c_j^\dagger$ and $\sigma_j^z = 2c_j^\dagger c_j - 1$, the Hamiltonian of Eq. (10) reads

$$H_0 = \sum_{ij} \left[c_i^\dagger A_{ij} c_j + \frac{1}{2} \left(c_i^\dagger B_{ij} c_j^\dagger + \text{H.c.} \right) \right], \quad (11)$$

where $A_{ij} = 2h[(1-\mu)\delta_{i1} - 1]\delta_{ij} + (\delta_{i,j+1} + \delta_{i+1,j}) = A_{ji}$ and $B_{ij} = (\delta_{i+1,j} - \delta_{i,j+1}) =$

$-B_{ji}$. Following [14, 60, 61], the Hamiltonian (11) can be brought to the form

$$H_0 = \sum_{\kappa} \Gamma_{\kappa} \gamma_{\kappa}^\dagger \gamma_{\kappa} + \text{const.}, \quad (12)$$

where $c_j = \sum_{\kappa} u_{j\kappa} \gamma_{\kappa} + v_{j\kappa} \gamma_{\kappa}^\dagger$ represents the Bogoliubov transformation [60]. γ_{κ} are fermionic degrees of freedom: $\gamma_{1,2}$ for the localized modes, and γ_k for the delocalized ones. To guarantee the correct fermionic anti-commutation relations, $\{\gamma_{\kappa}^\dagger, \gamma_{\kappa'}\} = \delta_{\kappa\kappa'}$ and $\{\gamma^\dagger, \gamma_{\kappa'}\} = 0$, the wave functions $u_{j\kappa}$ and $v_{j\kappa}$ need to satisfy (in matrix notation): $\mathbf{1} = uu^T + vv^T$ and $\mathbf{0} = uv^T + vu^T$, where $\mathbf{1}$ is the identity matrix, $\mathbf{0}$ is the null matrix and T denotes the transpose operation. The inverse transformation reads, $\gamma_{\kappa} = \sum_j u_{j\kappa} c_j + v_{j\kappa} c_j^\dagger$. In what follows, we will work with the quantities, $\psi_{j\kappa} \equiv u_{j\kappa} - v_{j\kappa}$ and $\phi_{j\kappa} \equiv u_{j\kappa} + v_{j\kappa}$.

As discussed in the main text, the localized edge modes $\gamma_{\ell=1,2}$ only appear in specific regions of the (h, μ) -phase diagram (see Fig. 1(b) in the main text). For the γ_2 mode, these regions are: $|\mu| > \sqrt{1+1/h}$ for all $h > 0$ and $|\mu| < \sqrt{1-1/h}$ for $h > 1$. The energy and wave functions of this mode are,

$$\begin{aligned} \Gamma^{(2)} &= 2|\mu| \sqrt{\frac{1 + (\mu^2 - 1)h^2}{\mu^2 - 1}}, \\ \psi_j^{(2)} &= \frac{(-1)^j h^{-j} \sqrt{(\mu^2 - 1)^2 h^2 - 1}}{(\mu^2 - 1)^j}, \\ \phi_j^{(2)} &= \frac{1}{\Gamma^{(2)}} \left[-2h\psi_j^{(2)} + 2h(1 - \mu)\delta_{j1}\psi_1^{(2)} \right. \\ &\quad \left. + 2(1 - \delta_{j1})\psi_{j-1}^{(2)} \right], \end{aligned} \quad (13)$$

where, hereafter, we use the superscript (ℓ) to label the localized mode $\ell = 1, 2$. The γ_1 mode exists in the entire region $h < 1$ (topological phase of the Kitaev chain [23]). For this mode, we have

$$\begin{aligned} \Gamma^{(1)} &\simeq \frac{2|\mu|(1-h^2)h^N}{\sqrt{1+h^2(\mu^2-1)}}, \\ \psi_j^{(1)} &= \sqrt{1-h^2}h^N \left(h^{-j} - \frac{\mu^2 h^j}{1+h^2(\mu^2-1)} \right), \\ \phi_j^{(1)} &= -\frac{\text{sgn}(\mu)\sqrt{1-h^2}\sqrt{1+h^2(\mu^2-1)}}{h[1+h^2(\mu^2-1)]} \\ &\quad \times [\delta_{j1}(1-\mu) + \mu]h^j. \end{aligned} \quad (14)$$

where $\text{sgn}\{\cdot\}$ is the sign function. Notice that in the limit $N \rightarrow \infty$, $\Gamma^{(1)}, \psi_1^{(1)} \rightarrow 0$.

Finally, for the delocalized modes γ_k , we have

$$\begin{aligned} \Gamma_k &= 2\sqrt{1+h^2-2h\cos k}, \\ \psi_{jk} &= \sqrt{\frac{2}{N}} \frac{\sin jk + h(\mu^2-1)\sin(j-1)k}{\sqrt{1+h^2(\mu^2-1)^2+2h(\mu^2-1)\cos k}}, \\ \phi_{jk} &= \frac{1}{\Gamma_k} \left[-2h\psi_{jk} + 2h(1-\mu)\psi_{1k}\delta_{j1} \right. \\ &\quad \left. + 2(1-\delta_{j1})\psi_{j-1,k} \right]. \end{aligned} \quad (15)$$

In the continuum limit, we can take $k \in [0, \pi]$ as usual [14]. We see that the system gap closes at $h = 1$, independently of μ , where the system undergoes a quantum phase transition [59].

Majorana representation

The model of Eq. (10) can be rewritten in terms of Majorana fermions. As discussed in the main text, this representation is useful for the calculation of the OTOC.

Decomposing the spinless fermionic operators c_i in the basis, $c_j^\dagger = \frac{a_j - ib_j}{2}$ and $c_j = \frac{a_j + ib_j}{2}$, where a_j and b_j are Majorana fermions, $a_j^2 = b_j^2 = 1$, $\{a_j, a_{j'}\} = \{b_j, b_{j'}\} = 2\delta_{jj'}$ and $\{a_j, b_{j'}\} = 0$, the Hamiltonian of Eq. (11) is recast as

$$H_0 = ih\mu b_1 a_1 + ih \sum_{j=2}^N b_j a_j - i \sum_{j=1}^{N-1} b_j a_{j+1} + \text{const.} \quad (16)$$

In particular, when $\mu = 0$, we can see that the Majorana fermion a_1 totally decouples from the rest of the chain, $[a_1, H_0] = 0$, and thus it becomes a Majorana zero mode. For $h < 1$, this mode is reminiscent of Kitaev's zero mode, while for $h > 1$, it is simply an impurity effect.

OTOC CALCULATION

Here, we are interested in the OTOC,

$$\begin{aligned} \mathcal{C}(t, \mu) &= \frac{1}{2} \langle |[\sigma_1^z(t), \sigma_1^z(0)]|^2 \rangle_0, \\ &= 1 - \text{Re}\{F(t, \mu)\}, \end{aligned} \quad (17)$$

where $F(t, \mu) = \langle \sigma_1^z(t) \sigma_1^z(0) \sigma_1^z(t) \sigma_1^z(0) \rangle_0$ and $\text{Re}\{\dots\}$ denotes the real part. Using the Majorana representation

$$\begin{aligned} 2^{-1} \mathcal{C}(t, \mu) &= (\text{Re}\{G_{ba}(t)\})^2 + (\text{Re}\{G_{ab}(t)\})^2 + (\text{Re}\{G_{aa}(t)\})^2 + (\text{Re}\{G_{bb}(t)\})^2 \\ &\quad - 2 \left[\text{Re}\{G_{ba}(t)\} \text{Re}\{G_{ab}(t)\} - \text{Re}\{G_{aa}(t)\} \text{Re}\{G_{bb}(t)\} \right] \left[\text{Re}\{G_{ab}^2(0)\} \right. \\ &\quad \left. + \text{Re}\{G_{ab}(t)\} \text{Re}\{G_{ba}(t)\} - \text{Im}\{G_{ab}(t)\} \text{Im}\{G_{ba}(t)\} \right. \\ &\quad \left. - \text{Re}\{G_{aa}(t)\} \text{Re}\{G_{bb}(t)\} + \text{Im}\{G_{aa}(t)\} \text{Im}\{G_{bb}(t)\} \right], \end{aligned} \quad (25)$$

where $\text{Im}\{\dots\}$ denotes the imaginary part.

The two-point Majorana correlation functions in the

discussed before, we can rewrite $\sigma_1^z = ia_1 b_1$ so that

$$F(t, \mu) = \langle a_1(t) b_1(t) a_1 b_1 a_1(t) b_1(t) a_1 b_1 \rangle_0. \quad (18)$$

The above OTOC can be calculated applying Wick's theorem since a_1 and b_1 are linear combinations of γ_κ and γ_κ^\dagger . However, as shown in reference [36], this expectation value can be cast in the form of a Pfaffian of a matrix $\mathcal{M}(t)$,

$$F(t, \mu) = \text{Pf}\{\mathcal{M}(t)\}. \quad (19)$$

For our case,

$$\mathcal{M}(t) = \begin{pmatrix} \mathcal{A}(0) & \mathcal{B}(t) & \mathbf{1} + \mathcal{A}(0) & \mathcal{B}(t) \\ -\mathcal{B}^\text{T}(t) & \mathcal{A}(0) & \mathcal{B}(-t) & \mathbf{1} + \mathcal{A}(0) \\ -\mathbf{1} + \mathcal{A}(0) & -\mathcal{B}^\text{T}(-t) & \mathcal{A}(0) & \mathcal{B}(t) \\ -\mathcal{B}^\text{T}(t) & -\mathbf{1} + \mathcal{A}(0) & -\mathcal{B}^\text{T}(t) & \mathcal{A}(0) \end{pmatrix}, \quad (20)$$

where we defined the 2×2 matrices

$$\mathcal{A}(t) = \begin{pmatrix} 0 & G_{ab}(t) \\ -G_{ab}(t) & 0 \end{pmatrix}, \quad (21)$$

$$\mathcal{B}(t) = \begin{pmatrix} G_{aa}(t) & G_{ab}(t) \\ G_{ba}(t) & G_{bb}(t) \end{pmatrix}. \quad (22)$$

Here, $G_{rr'}(t) \equiv \langle r(t) r'(0) \rangle_0$, where $r, r' = a_1, b_1$, and $\mathbf{1}$ is the 2×2 identity matrix. Notice that $\mathcal{A}(t) = -\mathcal{A}^\text{T}(t)$.

Since, like the determinant, the Pfaffian is invariant under the addition of rows and columns, we obtain

$$F(t, \mu) = \text{Pf}\{\tilde{\mathcal{M}}(t)\}, \quad (23)$$

where now

$$\tilde{\mathcal{M}}(t) = \begin{pmatrix} \mathcal{A}(0) & \mathcal{B}(t) & \mathbf{1} & \mathbf{0} \\ -\mathcal{B}^\text{T}(t) & \mathcal{A}(0) & \mathbf{0} & \mathbf{1} \\ -\mathbf{1} & \mathbf{0} & \mathbf{0} & \mathcal{B}(t) + \mathcal{B}^\text{T}(-t) \\ \mathbf{0} & -\mathbf{1} & -\mathcal{B}^\text{T}(t) - \mathcal{B}(-t) & \mathbf{0} \end{pmatrix}, \quad (24)$$

and $\mathbf{0}$ is the 2×2 null matrix. Performing the calculation, we find [36]

above expression, $G_{rr'}(t)$, are given by

$$\begin{aligned} G_{ab}(t) &= i \sum_{\kappa} \phi_{\kappa} \psi_{\kappa} e^{-i\Gamma_{\kappa} t}, \\ G_{ba}(t) &= [G_{ab}(-t)]^*, \\ G_{aa}(t) &= \sum_{\kappa} \phi_{\kappa}^2 e^{-i\Gamma_{\kappa} t}, \\ G_{bb}(t) &= \sum_{\kappa} \psi_{\kappa}^2 e^{-i\Gamma_{\kappa} t}, \end{aligned} \quad (26)$$

Region	$\Phi(Jt \gg 1, \mu)$	$\mathcal{C}(Jt \gg 1, \mu)$
$h > 1$ and $\mu \leq \sqrt{1 \mp 1/h}$	$t^{-3/2}$	Eq. (8)
$h > 1$ and $\mu = \sqrt{1 \mp 1/h}$	t^{-2}	t^{-1}
$h > 1$ and $\sqrt{1 - 1/h} < \mu < \sqrt{1 + 1/h}$	t^{-3}	t^{-3}
$h < 1$ and $\mu < \sqrt{1 + 1/h}$	$t^{-3/2}$	$\frac{2(1-h^2)^2}{[1+h^2(\mu^2-1)]^2} + \mathcal{O}(t^{-3/2})$
$h < 1$ and $\mu = \sqrt{1 + 1/h}$	$t^{-1/2}$	$2(1-h)^2 + \mathcal{O}(t^{-1/2})$
$h < 1$ and $\mu > \sqrt{1 + 1/h}$	Eq. (5)	$\propto 1 - (\text{const.}') \cos \Gamma^{(2)}t$

TABLE I. Asymptotic behaviors of the response function, Eq. (3), and the OTOC, Eq. (6), for the different boundary phases of the model in Eq. (1).

where the above summations include both the delocalized and the localized modes, and we used the notation $\psi_{1\kappa} \equiv \psi_\kappa$.

STATIONARY PHASE APPROXIMATION (SPA)

The long-time power-law behaviors observed for the response function and the OTOC (see Figs. 1 and 2 in the main text) can be understood by applying the stationary phase approximation (SPA) [30].

Response function $\Phi(t, \mu)$

In the limit $N \rightarrow \infty$, the summation over the bulk modes in Eq. (4) is converted to an integral. In the red region of Fig. 1(b), where we only have delocalized modes, the response function is given by

$$\Phi(t, \mu) = \int_0^\pi dk dk' f_{kk'} \sin[(\Gamma_k + \Gamma_{k'})t]. \quad (27)$$

The long-time limit ($t \gg J^{-1}$) of $\Phi(t, \mu)$ is obtained by performing the integration of $f_{kk'} \sin[(\Gamma_k + \Gamma_{k'})t]$ expanded near the extreme points of $\Gamma_k + \Gamma_{k'}$: $\{(0, 0), (0, \pi), (\pi, 0), (\pi, \pi)\}$ [see Eq. (15)]. Expanding around the points $\{(0, 0), (\pi, \pi)\}$ gives us $f_{kk'} \sim k^2 k'^2 (k^2 - k'^2)$, which produces a decay faster than t^{-3} . If we expand $f_{kk'}$ around $(0, \pi)$ (or, equivalently, around $(\pi, 0)$), we obtain $f_{kk'} \sim k^2 (k' - \pi)^2$. This leads to, $\Phi(t \gg J^{-1}, \mu) \sim (t^{-3/2})^2 = t^{-3}$, which agrees with the numerical calculation of Eq. (4), see Fig. 2(a, b).

When only one of the localized modes $\gamma_{\ell=1,2}$ is present (and far from the boundaries), besides the contribution in Eq. (27), we also have the term $\int_0^\pi dk (f_{k\ell} + f_{\ell k}) \sin[(\Gamma_k + \Gamma^{(\ell)})t]$. For the latter, obviously the extreme points are $k = 0, \pi$, and both of them give the same result, $f_{k\ell} \sim k^2$ (when expanded around $k = \pi$, we have done a π -translation). Thus, $\Phi(t \gg J^{-1}, \mu) \sim t^{-3/2}$. At the boundaries, $h > 1$ and $\mu = \sqrt{1 \mp 1/h}$, $f_{kk'}$ behaves as $f_{kk'} \sim k^2$ around $(0, \pi)$. Then, $\Phi(t \gg J^{-1}, \mu) \sim t^{-3/2} t^{-1/2} = t^{-2}$. However, at the boundary $\mu =$

$\sqrt{1 + 1/h}$ and $h < 1$, the mode γ_1 contributes, making $f_{k,\ell=1} \sim 1$ around $k = \pi$. This produces the slower decay seen in Fig. 2(c), $\Phi(t \gg J^{-1}, \mu) \sim t^{-1/2}$.

OTOC $\mathcal{C}(t, \mu)$

As we saw in the Sec. , to calculate $\mathcal{C}(t, \mu)$ we need to know the two-point Majorana correlation functions, $G_{rr'}(t)$, see Eq. (25). The long-time behavior of $G_{rr'}(t)$ can be extracted from the SPA discussed above. In the red region of Fig. 1(b), from Eq. (15) we obtain $\psi_k, \phi_k \sim k$ around $k = 0$. Thus, $G_{rr'}(t \gg J^{-1}) \sim t^{-3/2}$ (see Eq. (26)). This leads to $\mathcal{C}(t \gg J^{-1}, \mu) \sim t^{-3}$. At the boundaries $h > 1$ and $\mu = \sqrt{1 \mp 1/h}$, $\psi_k, \phi_k \sim 1$ (for $\mu = \sqrt{1 - 1/h}$ we have expanded around $k = 0$ while for $\mu = \sqrt{1 + 1/h}$ around $k = \pi$). Then, $G_{rr'}(t \gg J^{-1}) \sim t^{-1/2}$, which produces $\mathcal{C}(t \gg J^{-1}, \mu) \sim t^{-1}$.

In table I we summarize all the results for the asymptotic behaviors of $\Phi(t, \mu)$ and $\mathcal{C}(t, \mu)$.

REDUCED STATE FOR THE LOCALIZED MODES

For the system initially prepared in its ground state $|\mathbf{0}\rangle$ within the yellow region of Fig. 1(b), we turn on the impulsive perturbation $-g_0 \delta(t) \sigma_1^z$. The system state at time $t > 0$ will be given by

$$|\Psi(t)\rangle = e^{-iH_0 t} T \exp \left[-i \int_0^t dt' \delta H(t') \right] |\mathbf{0}\rangle, \quad (28)$$

where $\delta H(t) = -g_0 \delta(t) \sigma_1^z(t)$, with $\sigma_1^z(t) = e^{iH_0 t} \sigma_1^z e^{-iH_0 t}$, and T is the time ordering operator. Using the Dirac delta function property,

$$|\Psi(t)\rangle = (\cos g_0 \mathbf{1} + i \sin g_0 e^{-iH_0 t} \sigma_1^z) |\mathbf{0}\rangle, \quad (29)$$

where it was considered that $H_0|0\rangle = 0$. Thus, the system density operator reads,

$$\begin{aligned}\rho(t) &= |\Psi(t)\rangle\langle\Psi(t)|, \\ &= \cos^2 g_0 (|0\rangle\langle 0|) - i\frac{\sin 2g_0}{2} (|0\rangle\langle 0|\sigma_1^z e^{iH_0 t}), \\ &\quad + i\frac{\sin 2g_0}{2} (e^{-iH_0 t}\sigma_1^z |0\rangle\langle 0|), \\ &\quad + \sin^2 g_0 (e^{-iH_0 t}\sigma_1^z |0\rangle\langle 0|\sigma_1^z e^{iH_0 t}).\end{aligned}\quad (30)$$

The density operator $\rho(t)$, being the state of the full system, provides the time evolution of any average value, in particular, the local magnetization of the impurity, given by $\langle\sigma_1^z(t)\rangle$. However, $\langle\sigma_1^z(t)\rangle$ can also be obtained from the response function (3) in the perturbative regime and, as shown in Fig.2(c) of the manuscript, its long-time behavior has persistent oscillations when the two localized modes are present. Next, we show that this is a signature of the X -state in the reduced density operator of the localized modes and that couplings (in the sense of non-diagonal matrix elements of $\rho(t)$) introduced by the perturbation between the edge and bulk modes with different number of excitations in the later ones decay in the long-time limit. To see this, we express $\langle\sigma_1^z(t)\rangle$ as follows,

$$\begin{aligned}\langle\sigma_1^z(t)\rangle &= \text{Tr}\{\rho(t)\sigma_1^z\}, \\ &= \sum_{n,n'} \langle n|\rho(t)|n'\rangle \langle n'|\sigma_1^z|n\rangle,\end{aligned}\quad (31)$$

where $|n\rangle$ and $|n'\rangle$ are two Fock states: $|n\rangle \equiv |n_1, n_2\rangle \otimes |\nu_1, \nu_2, \dots\rangle$, being $|n_1, n_2\rangle$ (with $n_{\ell=1,2} = 0, 1$) the lo-

calized edge modes part and $|\nu_1, \nu_2, \dots\rangle$ (with $\nu_i = 0, 1$) the delocalized modes part. Because σ_1^z creates zero or two γ_κ excitations ($\sigma_j^z = 2c_j^\dagger c_j - 1$), the non-zero terms in the above expression are terms where $|n\rangle$ and $|n'\rangle$ differ by zero or two excitations. These excitations can occupy edge or bulk modes. However, in the long-time limit, $t \gg J^{-1}$, not all of those terms will survive due to the presence of high oscillatory factors. For instance, let us analyze the matrix elements $\langle kk' | \otimes \langle 0, 0 | \rho(t) | 1, 0 \rangle \otimes |k''\rangle$, where $|k\rangle = \gamma_k^\dagger |0_d\rangle$ and $|kk'\rangle = \gamma_k^\dagger \gamma_{k'}^\dagger |0_d\rangle$, being $|0_d\rangle$ the delocalized fermionic vacuum, $\nu_i = 0$. The last term of Eq. (30) gives us (the others are zero),

$$\langle kk' | \otimes \langle 0, 0 | \rho(t) | 1, 0 \rangle \otimes |k''\rangle \sim e^{-i(\Gamma_k + \Gamma_{k'} - \Gamma_{k''})t}.\quad (32)$$

Thus, the sum over all states like this in Eq. (31), is a sum of high oscillatory terms, which goes to zero when $t \gg J^{-1}$. Therefore, the only surviving coherences in the long-time limit are those corresponding to Fock states with equal number of excitations in the bulk modes. In the long-time limit, the relevant content of $\rho(t)$ is hence concentrated in the subspace spanned by the states with 0, 1 and 2 excitations in the edge modes, i.e., in the reduced density operator obtained by

$$\begin{aligned}\rho_{\text{loc}}(t) &= \text{Tr}_{\text{del}} \rho(t), \\ &= \sum_{\nu_1, \nu_2, \dots} \langle \nu_1, \nu_2, \dots | \rho(t) | \nu_1, \nu_2, \dots \rangle.\end{aligned}\quad (33)$$

After performing the above calculation, we find

$$\begin{aligned}\rho_{\text{loc}}(t) &= \rho_{11}|0, 0\rangle\langle 0, 0| + \rho_{22}|1, 0\rangle\langle 1, 0| + \rho_{33}|0, 1\rangle\langle 0, 1| + \rho_{44}|1, 1\rangle\langle 1, 1|, \\ &\quad + \rho_{14}(t)|0, 0\rangle\langle 1, 1| + \rho_{14}^*(t)|1, 1\rangle\langle 0, 0| + \rho_{23}(t)|1, 0\rangle\langle 0, 1| + \rho_{23}^*(t)|0, 1\rangle\langle 1, 0|.\end{aligned}\quad (34)$$

In the matrix representation this reads,

$$\rho_{\text{loc}}(t) = \begin{pmatrix} \rho_{11} & 0 & 0 & \rho_{14}(t) \\ 0 & \rho_{22} & \rho_{23}(t) & 0 \\ 0 & \rho_{23}^*(t) & \rho_{33} & 0 \\ \rho_{14}^*(t) & 0 & 0 & \rho_{44} \end{pmatrix},\quad (35)$$

where

$$\rho_{11} = \cos^2 g_0 + \sin^2 g_0 \left[|\Upsilon_1|^2 + \sum_{kk'(k \neq k')} |\Upsilon_2(k, k')|^2 \right],$$

$$\begin{aligned}\rho_{22} &= \sin^2 g_0 \sum_k |\Upsilon_3(k)|^2, \\ \rho_{33} &= \sin^2 g_0 \sum_k |\Upsilon_4(k)|^2, \\ \rho_{44} &= \sin^2 g_0 |\Upsilon_5|^2, \\ \rho_{14}(t) &= \Upsilon_5^* \left[-i\frac{\sin 2g_0}{2} + \Upsilon_1 \sin^2 g_0 \right], \\ \rho_{23}(t) &= \sin^2 g_0 \sum_k \Upsilon_3(k) \Upsilon_4^*(k).\end{aligned}\quad (36)$$

The functions Υ_i in the above expressions are

$$\begin{aligned}
\Upsilon_1 &= -1 + 2 \sum_k v_k^2, \\
\Upsilon_2(k, k') &= 2e^{-i(\Gamma_k + \Gamma_{k'})t} v_{k'} u_k, \\
\Upsilon_3(k) &= 2e^{-i(\Gamma_k + \Gamma^{(1)})t} [v^{(1)} u_k - v_k u^{(1)}], \\
\Upsilon_4(k) &= 2e^{-i(\Gamma_k + \Gamma^{(2)})t} [v^{(2)} u_k - v_k u^{(2)}], \\
\Upsilon_5 &= 2e^{-i(\Gamma^{(2)} + \Gamma^{(1)})t} [v^{(2)} u^{(1)} - v^{(1)} u^{(2)}].
\end{aligned} \tag{37}$$

Notice that Υ_1 is time-independent.

PURITY, ENTANGLEMENT AND DISCORD

The purity is obtained as usual from $\text{Tr}_{\text{loc}} \rho_{\text{loc}}^2(t)$, with $\rho_{\text{loc}}(t)$ given by Eq. (9). The entanglement measure is given by the concurrence, $0 < C(\rho_{\text{loc}}(t)) < 1$, which can be obtained in terms of the matrix elements of the X -state as follows [48]

$$\begin{aligned}
C(\rho_{\text{loc}}(t)) &= \\
&\max\{0, 2(|\rho_{14}(t)| - \sqrt{\rho_{22}\rho_{33}}), 2(|\rho_{23}(t)| - \sqrt{\rho_{11}\rho_{44}})\}.
\end{aligned} \tag{38}$$

Finally, the discord is obtained following Refs. [48, 53]. In Figs. 5 and 6 we show the results for these three quantities assuming different h values.

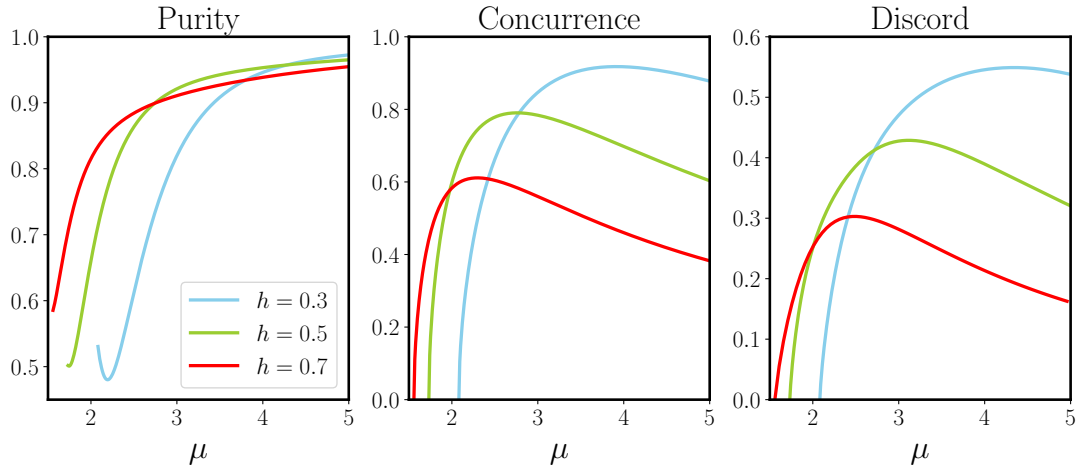


FIG. 5. Purity, concurrence and discord for the X -state in Eq. (9). The lower μ cutoffs of the purity curves come from the need to satisfy $\mu > \sqrt{1 + 1/h}$. Here we take $g_0 = 0.5$.

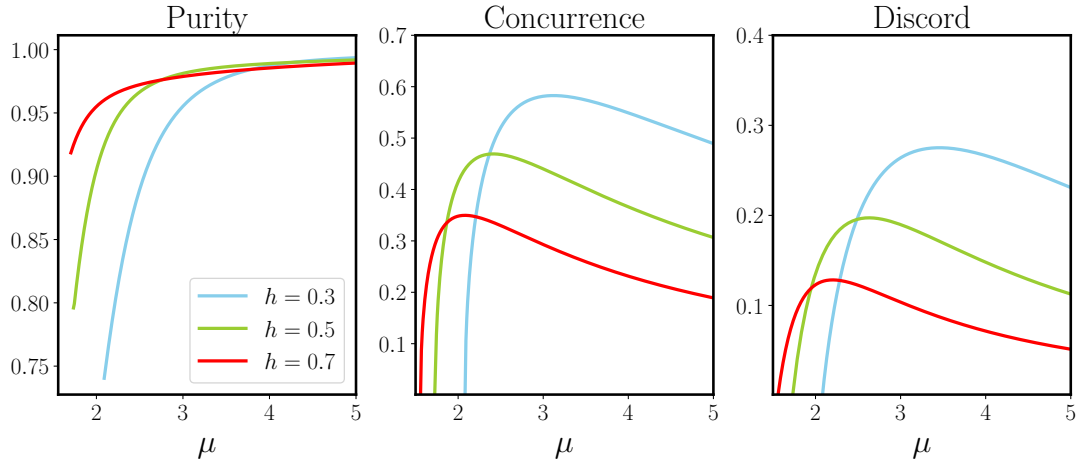


FIG. 6. Purity, concurrence and discord for the X -state in Eq. (9). The lower μ cutoffs of the purity curves come from the need to satisfy $\mu > \sqrt{1 + 1/h}$. Here we take $g_0 = \pi/2$.